Optical Single-Channel Analysis of the Aerolysin Pore in Erythrocyte Membranes

Mathias Tschödrich-Rotter,* Ulrich Kubitscheck,* Gabriele Ugochukwu,* J. Thomas Buckley,[‡] and Reiner Peters*

*Institut für Medizinische Physik und Biophysik, Westfälische Wilhelms-Universität, 48149 Münster, Germany, and ‡Department of Biochemistry and Microbiology, University of Victoria, Victoria, BC V8W 3P6 Canada

ABSTRACT   Scanning microphotolysis (Scamp), a recently developed photobleaching technique, was used to analyze the transport of two small organic anions and one inorganic cation through single pores formed in human erythrocyte membranes by the channel-forming toxin aerolysin secreted by *Aeromonas* species. The transport rate constants of erythrocyte ghosts carrying a single aerolysin pore were determined to be $(1.83 \pm 0.43) \times 10^{-3}$ s^{-1} for Lucifer yellow, $(0.33 \pm 0.10) \times 10^{-3}$ s^{-1} for carboxyfluorescein, and $(8.20 \pm 2.30) \times 10^{-3}$ s^{-1} for Ca^{2+}. The radius of the aerolysin pore was derived from the rate constants to be 19-23 Å, taking steric hindrance and viscous drag into account. The size of the Ca^{2+} rate constant implies that at physiological extracellular Ca^{2+} concentrations (>1 mM) the intracellular Ca^{2+} concentration would be elevated to the critical level of >1 μM in much less than a second after formation of a single aerolysin pore in the plasma membrane. Thus changes in the levels of Ca^{2+} or other critical intracellular components may be more likely to cause cell death than osmotic imbalance.

INTRODUCTION

Aerolysin is a member of the family of pore-forming cytolytic proteins employed by many microorganisms and eukaryotic cells to attack target membranes (for a review, see Menestrina, 1994). The protein is secreted by several pathogenic *Aeromonas* species as an inactive protoxin comprising 470 residues (reviewed in van der Goot et al., 1994). Proteolytic cleavage at the C-terminus produces the active toxin (427 residues), which is able to oligomerize and insert into biological membranes, leading to the formation of well-defined channels that are thought to cause death by disturbing the ionic and osmotic balance of the cell.

Fluorescence microphotolysis, also referred to as fluorescence recovery after photobleaching (Jacobson et al., 1976) or fluorescence photobleaching recovery (Axelrod et al., 1976), was initially introduced to study the lateral mobility of lipids and proteins in cellular membranes (Peters et al., 1974). The method was later extended to the transport of fluorescent compounds across membranes in single cells and organelles (for a review, see Peters and Scholz, 1991). By application to cells carrying only very few pores it was shown that fluorescence microphotolysis could be used to measure transport through single-membrane transporters (optical single-channel analysis, OSCA; Peters et al., 1990).

OSCA was initially based on microscopic measurements performed cell by cell. This is a time-consuming procedure because OSCA requires large numbers of individually measured values, as does any statistical analysis. Consequently,

only two types of pores have been studied using OSCA, those formed by perforin (Peters et al., 1990) and by complement (Sauer et al., 1991), and only a single probe, Lucifer yellow (LY), has been used.

The ease of data acquisition has recently been greatly improved (Wedekind et al., 1994) by the development of scanning microphotolysis (Scamp). In this procedure, a confocal laser scanning microscope (CLSM) is complemented with a device called the Scamper, which makes it possible to switch the laser beam on and off during scanning according to a predefined image mask. As a result almost any pattern can be bleached into fluorescent samples, and changes with time can be followed by repetitive confocal imaging. Because this allows the measurement of transport after photolysis in up to 100 cells simultaneously, data of much better quality can be obtained in much shorter times. What is more, the range of applications of OSCA has broadened with the availability of increasing numbers of fluorescent ion indicators and photolabile or caged compounds, which enable single-cell flux measurements of non-fluorescent transport substrates such as Ca^{2+} (Kubitscheck et al., 1995).

In the present study, the new technical advances have been exploited to subject the aerolysin pore in human erythrocyte membranes to single-channel analysis. The fluxes of two anionic fluorescent dyes of different sizes, LY and carboxyfluorescein (CF), were measured, as was the flux of Ca^{2+}, a cation of central physiological importance. The results have implications for both the structure and function of the aerolysin pore.

THEORETICAL CONCEPTS

This section briefly summarizes the theoretical concepts of OSCA described previously in detail (Peters, 1983, 1984;

Peters et al., 1990). It also provides equations for Ca^{2+} transport measurements.

Relationship between intracellular concentration and fluorescence signal

Fluorescent transport substrate

For passive transport into cells dispersed in an infinite volume, the time development of the internal concentration $c(t)$ of a particular transport substrate is given by

$$\frac{c(\infty) - c(t)}{c(\infty) - c(0)} = e^{-kt}, \tag{1}$$

where $c(\infty)$ is the intracellular concentration at equilibrium, $c(0)$ is the intracellular concentration at zero time, and k is the transport rate constant. If the transport of a fluorescent transport substrate is measured at low concentrations it can be assumed that the fluorescence signal $F(t)$, measured by confocal microscopy and corrected for dark current and autofluorescence, is directly proportional to $c(t)$. Then

$$\frac{F(t) - F(0)}{F(\infty) - F(0)} = 1 - e^{-kt}. \tag{2}$$

Nonfluorescent transport substrate

If the transport substrate is not fluorescent, its concentration can be measured by using a suitable fluorescent indicator. In addition, a photolabile (caged) precursor of the substrate is required to generate a sudden concentration jump by microphotolysis. In this case the analysis is more complex than with a fluorescent substrate because i) the substrate buffering characteristics of the indicator dye have to be taken into account and ii) the relation between concentration and fluorescence is nonlinear. The analysis is here presented for calcium, employing calcium green (CG) as the indicator.

The calcium export by passive diffusion is governed by the following differential equation:

$$\frac{dCa_{tot}}{dt} = - k \cdot Ca_{free}, \tag{3}$$

where the total and free calcium concentrations are designated by Ca_{tot} and Ca_{free}, respectively. Using the mass action law describing the binding of calcium to CG, and the mass conservation equations for CG and Ca, Ca_{tot} could be written as a function of Ca_{free}. From this, the derivative dCa_{tot}/dCa_{free} was obtained. Replacing dCa_{tot}/dt in Eq. 3 by $dCa_{tot}/dCa_{free} \cdot dCa_{free}/dt$, and inserting dCa_{tot}/dCa_{free} yielded

$$\frac{dCa_{free}}{dt} = \frac{- k \cdot Ca_{free}}{1 + \dfrac{K_d \cdot CG_{tot}}{(K_d + Ca_{free})^2}}, \tag{4}$$

where K_d designates the dissociation constant of the calcium-indicator complex, and CG_{tot} the total concentration of

CG. Approximation of the right-hand side of Eq. 4 up to second order resulted in a Bernoulli differential equation. This could be solved by standard means, yielding

$$Ca_{free}(t) = [b' \cdot e^{gkt} - f]^{-1}. \tag{5}$$

Here, g and f are constants depending on K_d and CG_{tot}, which were determined by the approximation mentioned above. b' is given by $f + 1/Ca_{free}(0)$. With $K_d = 0.3 \ \mu M$ for the dissociation constant of CG (Kubitscheck et al., 1995) and $CG_{tot} = 20 \ \mu M$, the concentration used in our experiments, $g = 0.2616$ and $f = 0.455 \ \mu M^{-1}$. To verify the validity of the approximation to Eq. 4, Eq. 4 was numerically integrated with a fifth-order Runge-Kutta method, and the result was compared to the approximate solution given by Eq. 5. This control clearly proved the validity of our approach.

Employing a fluorescent calcium indicator such as CG the relation between fluorescence signal and Ca^{2+} concentration is given (Tsien et al., 1984) by

$$Ca_{free}(t) = K_d \cdot \frac{F(t) - F_{min}}{F_{max} - F(t)}, \tag{6}$$

where F_{min} is the fluorescence signal in the absence of calcium and F_{max} is the fluorescence signal with an excess of calcium (i.e., calcium concentration $\gg K_d$). Insertion of Eq. 5 into Eq. 6 yields

$$\frac{(Ft) - F_{min}}{F_{max} - F(t)} = \frac{1}{b \ e^{0.2616 \ kt} - 0.136}. \tag{7}$$

This expression was used to describe our experimental results using b and K as free fitting parameters.

Relations between rate constant, permeability coefficient, and flux per single pore

The flux Φ of the transport substrate, i.e., the number of particles transported across the membrane of a vesicle per time, is given by

$$\Phi = P(n) \cdot A \cdot \Delta C, \tag{8}$$

where $P(n)$ is the permeability coefficient of the membrane, here a function of the number of pores per cell, n. A is the membrane area of the vesicle, and ΔC is the concentration difference of the substrate across the membrane. The relation between permeability coefficient and rate constant, $k(n)$, is given by

$$P(n) = k(n) \cdot V/A, \tag{9}$$

with V being the volume of the cell. Thus

$$\Phi = V \cdot k(n) \cdot \Delta C. \tag{10}$$

Passive diffusional transport of spherical molecules through cylindrical pores

In the case of passive, diffusional transport of spherical molecules through cylindrical pores the rate constant $k(n)$ is related (Peters, 1984) to the diffusion coefficient D of the transport substrate in the pore, the effective cross-sectional area A_{eff} of the pore, and the pore length Δx by

$$k(n) = n \cdot \frac{D \cdot A_{eff}}{\Delta x \cdot V} = n \cdot k(1). \tag{11}$$

Thus, the rate constant $k(n)$ is expected to be directly proportional to the number of pores per ghost, n, and to occur in discrete multiples of $k(1)$, the rate constant of ghosts with a single pore.

Single-channel analysis

In reality $k(1)$ will not have a single value but rather will be a gaussian distribution around a mean value μ_1 with a standard deviation σ_1 caused by variations in channel geometry, cell volume, etc. Therefore we model $k(n)$ by a gauss function G_n (Peters et al., 1990):

$$G_n = \frac{1}{\sigma_n \sqrt{2\pi}} e^{(k(n) - \mu_n)^2/2\sigma_n^2}, \tag{12}$$

where $\sigma_n = \sqrt{n \cdot \sigma_1^2}$ and $\mu_n = n \cdot \mu_1$ are the standard deviation and the mean value of G_n. We can assume, furthermore, that the generation of pores is a random process. Then the distribution $P(n)$ of the pore number n in the cell population is given by the Poisson distribution

$$P(n) = \frac{\lambda^n}{n!} \cdot e^{-\lambda}, \tag{13}$$

where λ is the mean value. The probability $p(k)$ is then given by

$$p(k) = \sum P(n) \cdot G_n. \tag{14}$$

Calculation of the pore radius

Rearrangement of Eq. 11 yields for the effective pore radius r_{eff}

$$r_{eff} = \sqrt{(k(1) \cdot \Delta x \cdot V)/(\pi \cdot D)}. \tag{15}$$

The effective pore radius r_{eff} would be only identical with the true, geometric pore radius r if the probe molecule is much smaller than r. This is not given in the present case. However, a radius r_o that is corrected for steric hindrance at the pore entrance and viscous drag inside the pore (but not for the effect of fixed charges) can be derived from r_{eff} (Pappenheimer et al., 1951; Renkin, 1954; Paine and Scherr, 1975) by

$$\frac{r_{eff}}{r_o} = (1 - \frac{a}{r_o})/\sqrt{\kappa_1}, \tag{16}$$

where a is the effective molecular radius of the probe molecule and κ_1 is a tabulated parameter (Paine and Scherr, 1975).

MATERIALS AND METHODS

Reagents and solutions

Phosphate-buffered saline contained 150 mM NaCl, 5 mM Na_2HPO_4, pH 7.4. KCl buffer contained 160 mM KCl, 20 mM HEPES, pH 7.4 and "lysis solution" consisted of 5 mM $MgSO_4$, 0.4 mM acetic acid, pH 4.2. LY and CF were obtained from Molecular Probes (Eugene, OR). Stock solutions were 3 mg/ml (LY) and 1 mg/ml (CF) in KCl buffer. The Ca^{2+} transport solution contained 100 μM CG (Molecular Probes), 1.0 mM [1-(2-nitro-4,5-dimethoxyphenyl-)-1,2-diaminoethane-N,N,N',N'-tetraacetic acid (DMN; Calbiochem-Novabiochem, Bad Soden, Germany), 125 μM $CaCl_2$, 2.0 mM reduced glutathione, 20 mM HEPES, 160 mM KCl. Glutathione was added following a recommendation of Kaplan et al. (1978) to trap nitrosoketones that might arise during the photolysis of DMN.

Proaerolysin was purified as described previously (Buckley, 1990). The protoxin (1 mg/ml) was activated by mixing 10 μl of the pro-aerolysin stock solution with 1 μl of a trypsin solution (1 mg/ml) and 89 μl of KCl buffer. The mixture was incubated for 60 min at room temperature and then stored on ice for further use.

The activity of aerolysin was tested by a hemolytic assay as described previously (Howard and Buckley, 1982). In short, a geometrical dilution series of an aerolysin solution of known concentration was prepared employing a multititer plate. Then to each well an aliquot of a 2% suspension of washed erythrocytes was given, and the plate was incubated for 1 h at 37°C. In that time span ghosts that had acquired at least one pore were lysed, an effect easily recognized by visual inspection of the microtiter plate. In wells with an aerolysin concentration sufficiently large to lyse the erythrocytes a clear red solution was seen, whereas in wells with an aerolysin concentration too small to cause the generation of at least one pore per ghost the erythrocytes had settled on the bottom. Thus, the aerolysin concentration inducing the formation of about one pore per cell could be easily determined.

Control experiments were performed to make sure that during the 60-min incubation, used routinely for activation of aerolysin, aerolysin was not degraded. In these experiments the incubation time was reduced to 10 min, and the reaction was then stopped by adding a surplus of trypsin inhibitor. When employing the hemolytic assay, no differences in activity were detected between preparations activated for 60 min or 10 min.

Erythrocyte ghosts

Human erythrocyte ghosts were prepared according to the method of Schwoch and Passow (1973) as recently described (Kubitscheck et al., 1995). Briefly, 0.7 ml of a 50% (v/v) suspension of washed human erythrocytes was added to 30 ml of lysis solution and incubated for 15 min while gently stirring. Then the ghosts were sedimented (16,000 × g, 20 min, 0°C), resuspended in 30 ml KCl buffer, again sedimented, and finally resuspended in KCl buffer to a final volume of 1.75 ml. At this stage the ghosts had lost most of their hemoglobin and were still permeable to small and large molecules. Additional steps depended on whether transport measurements involved a fluorescent or a nonfluorescent substrate:

i) For experiments involving LY or CF, ghosts were resealed by incubation at 37°C for 45 min. Aerolysin pores were generated by incubating 100 μl of resealed ghosts with a few microliters of activated aerolysin solution and KCl buffer in a total volume of 1.0 ml for 20 min at 37°C. The concentration of aerolysin was chosen on the basis of the hemolytic assay referred to above and amounted to approximately 50 ng/ml. After incubation, the ghosts were washed twice with KCl, and 97 μl of the suspension was mixed with 3 μl of LY (3 mg/ml) or CF (1 mg/ml).

ii) For measurements of Ca^{2+} transport 0.4 ml of the still-permeable ghosts kept on ice was mixed with 0.1 ml of Ca^{2+} transport solution. The

mixture was kept on ice for a further 10 min and then at 37°C for 45 min. Aerolysin pores were generated by mixing 100 μl of resealed ghosts with 5 μl of activated aerolysin and 895 μl of KCl buffer and incubating the mixture for 20 min at 37°C. Ghosts were then washed twice with KCl buffer.

Transport measurements

Transport measurements consisted of three steps: i) acquisition of confocal images of ghosts in both the fluorescence and transmitted light mode before photolysis (prebleach images), ii) photobleaching of fluorescent tracers or release of Ca^{2+}, and iii) acquisition of 5 to 15 fluorescence images at various times after photolysis (monitor images).

Ghost suspensions were loaded into "microslides," i.e., flattened glass capillaries with inner dimensions of 0.05 mm × 1 mm × 30 mm. After 20 min most of the ghosts had spontaneously adsorbed to the lower internal glass surface. The microslides were then sealed at the ends with silicon paste and mounted upside down (i.e., the layer of adsorbed ghosts on the upper side) on glass microslides. A microslide with a layer of adsorbed ghosts was placed on the stage of a confocal laser scanning microscope (CLSM or TCS; Leica, Heidelberg, Germany), and the image was focused so that the focal plane coincided with the center of the ghost layer, employing a 40-fold oil-immersion objective lens of 1.3 numerical aperture. The depth of focus was adjusted to be ≤1 μm by means of the confocal aperture. The 488-nm line of an argon laser was used for excitation, reducing the beam power to a degree at which the reduction of intracellular fluorescence was <0.5% per image. Care was taken to adjust the offset and the photomultiplier voltage in such a way that the measured signal was linearly related to the fluorescence intensity and so that the dynamic range of the instrument (256 gray levels) was optimally utilized.

Photobleaching of LY or CF was carried out by means of the Scamper (Wedekind et al., 1994) by placing a small window around each ghost and then bleaching this window at a sufficiently high laser power (cf. Fig. 1). Ca^{2+} was released by irradiating the scanned field through the vertical illuminator with the light of a 100-W high-pressure mercury lamp, isolating the 366-nm line by appropriate filters. The vertical illuminator was adjusted so that irradiated and imaged areas were approximately coincident. A photo shutter was integrated into the irradiation pathway to limit the irradiation time to 1/4 s, sufficient to decompose most of the caged compounds (Kubitscheck et al., 1995).

Data evaluation

To evaluate the images in terms of the time-dependent relative intracellular fluorescence intensities, we created a special computer program module. The module allowed us to place an arbitrary number of work windows in the image using the trackball of the microscope workstation. The work windows were adjusted to a size of ~2.5 μm × 2.5 μm, and they were placed in the centers of individual ghosts. Thus the relative fluorescence intensity originating from an intracellular volume of about 6 fl (2.5 μm × 2.5 μm × 1.0 μm) was obtained cell by cell. For analysis of a complete time series of images it was sufficient to set the work windows once. The program then automatically scanned through the image stack, extracting the time-dependent fluorescence data. The values for the intracellular fluorescence intensities obtained in this manner where then corrected for photobleaching and dark counts, both of which were minor parameters.

The transport rate constant k was determined for each ghost individually. In the case of LY or CF the data on the time course of the intracellular fluorescence were plotted according to Eq. 2 as $[F(t) - F(0)]/[[F(\infty) - F(0)]$, and this was fitted by a single-exponential $1 - e^{-kt}$ using a least-squares minimization routine. In the case of Ca^{2+} transport measurements, the data were plotted according to Eq. 7 as $[F(t) - F_{min}]/[F_{max} - F(t)]$, and fitted by $[b \cdot e^{0.2616 \cdot k \cdot t} - 0.136]^{-1}$.

The ensembles of k-values, consisting of 130–680 individual values (cf. Table 1), were plotted in the form of histograms as shown in Figs. 3, 4, and 7. The number of k-values within an interval of $\Delta k = 1 \times 10^{-3}$ s^{-1} (LY,
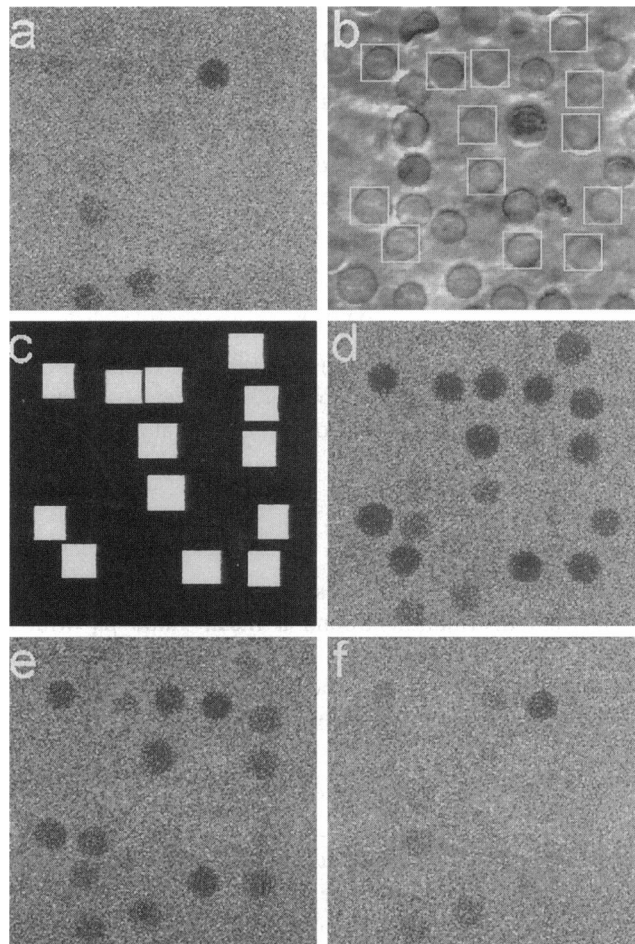

FIGURE 1   Scanning microphotolysis experiment to measure the membrane transport of Lucifer yellow (LY), a small hydrophilic fluorescent organic anion. Resealed human erythrocyte ghosts were treated with a limiting concentration of aerolysin to create approximately 1 pore/cell and then immersed in a solution of LY. (a) Confocal fluorescence image of ghosts before photolysis. Only ghosts without pores, thereby able to exclude LY, can be recognized. (b) Transmitted light images of the same field showing all ghosts together with the image mask used for photolysis. (c) Fluorescence image acquired during the photobleaching process. The laser beam is switched on only inside the selected areas shown in b. (d–f) Images taken at 0, 15, and 30 min after photobleaching. The depletion of ghosts from LY fluorescence and the influx of fresh LY into ghosts can be recognized.

Ca^{2+}) or 0.1×10^{-3} s^{-1} (CF) was counted, and this occupancy $p(k)$ was plotted versus k. The histograms were then smoothed by applying a mean filter ($n = 7$).

RESULTS

Single-channel permeability of the aerolysin pore to Lucifer yellow and carboxyfluorescein

Resealed human erythrocyte ghosts were exposed to aerolysin so that they carried approximately 1 pore/ghost on average. Then either LY or CF was added to the ghost suspension. Both tracers are dianions at the conditions employed, although they differ in molecular weight, shape, and

TABLE 1 Results of the optical single-channel analysis of the aerolysin pore in erythrocyte membranes

	Lucifer yellow	Carboxy-fluorescein		Ca^{2+}
Mean no. of pores per cell	1.17	1.00	0.56	1.58
Single-channel rate constant* $(10^{-3}$ $s^{-1})$	1.83 ± 0.43	0.33 ± 0.10	7.80 ± 1.85	8.20 ± 2.30
No. of measure-ments	260	130	170	670

*The rate constant for ghosts with a single pore is given as mean ± SD.

effective radius (7.8 Å versus 10 Å, cf. Table 2). After equilibration, a small volume of the ghost suspension was loaded into a microslide, and a confocal laser scanning microscope equipped for the Scamp method (Wedekind et al., 1994) was used to generate confocal images of ghosts adhering spontaneously to the glass-water interface.

This and the rest of the procedure are illustrated for the case of LY in Fig. 1. Before photolysis, images were taken in both the fluorescence (Fig. 1 a) and the transmission (Fig. 1 b) modes. Fig. 1 a shows that not all of the ghosts were permeable to LY, i.e., some did not carry at least one pore. This was expected and desired. The Poisson distribution (Eq. 13) predicts, for instance, that the fraction of ghosts without a pore is e^{-1} for a mean of 1 pore/ghost. Using the transmission image as a matrix, a number of ghosts was selected by enclosing them with small quadratic windows (Fig. 1 b). Then the Scamp process was initiated. This involved scanning the specimen at a laser beam power sufficiently large to cause rapid photobleaching of LY fluorescence. Instead of bleaching the scanned area homogeneously, the laser beam was only switched on when inside the selected areas. This can be directly observed in Fig. 1c, which was acquired during the bleaching scan. Spatially confined in that manner, photobleaching caused the fluorescence inside selected ghosts, but not in the medium surrounding the ghosts, to become largely diminished (Fig. 1 d). The influx of LY into bleached ghosts from the medium was then monitored by a series of confocal images, examples of which are shown in Fig. 1, e and f. These show that the influx kinetics varied considerably among different ghosts. It may be mentioned here that Fig. 1 contains "only" 13 windows, thus yielding 13 parallel flux measurements. This was done only so that ghosts and windows could be displayed at high magnification. Normally much larger fields were scanned and up to 100 flux measurements made in parallel.

The images series, consisting typically of a transmission and a fluorescence scan acquired before photolysis and

5–15 fluorescence scans acquired after microphotolysis in an interval of 900 s, were evaluated for the intracellular fluorescence of single ghosts. Fig. 2 shows experimental values (symbols) as well as best fits according to Eq. 2 (lines) for three ghosts selected from Fig. 1. The transport rate constants for the ghosts shown were $k = 1.9 \times 10^{-3}$, 3.8×10^{-3}, and 5.6×10^{-3} s^{-1}, respectively, which closely correspond to the mean k-values for ghosts with 1, 2, and 3 pores (see below).

When a large number of rate constants had been acquired in the described manner, a histogram was constructed (Fig. 3) by plotting the number of k-values found within a given k interval versus k (for details, see Materials and Methods). The experimental values (bars), consisting of 260 measurements, clearly exhibited discrete peaks, indicative of subpopulations of ghosts with different pore numbers. The first two peaks, corresponding to ghosts with 1 and 2 pores, respectively, are clearly resolved. Peaks corresponding to higher pore numbers disappear in the noise because the standard deviation increases (Eq. 12), whereas the occupancy decreases (Eq. 13) with the pore number. The experimental data could be well fitted by Eq. 14 (line). The fit yielded values (Table 1) for the rate constant of ghosts with a single pore $k(1) = (1.83 \pm 0.43) * 10^{-3}$ s^{-1} and the mean number of pores per ghost of $\lambda = 1.17$.

The transport of CF was analyzed in the very same manner. One hundred thirty k-values were collected and plotted as a histogram (Fig. 4). The experimental values (bars) showed two peaks that could be fit well by Eq. 14 (line). The transport rate $k(1)$ was found to be much smaller than that of LY, amounting to $(0.33 \pm 0.10) * 10^3$ s^{-1} (Table 1).
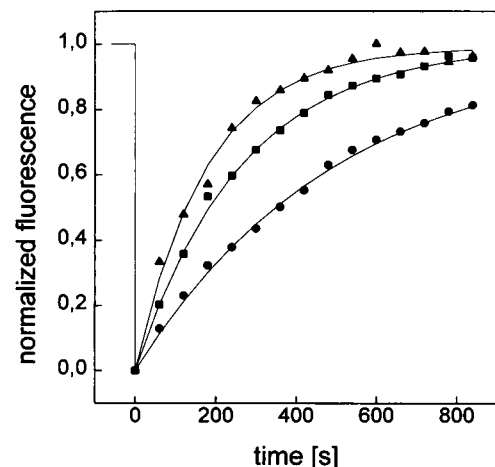

FIGURE 2 Examples of single-cell measurements to determine the transport rate constant for LY. A series of confocal images as shown in Fig. 1 was evaluated for the intracellular fluorescence of individual ghosts. The intracellular fluorescence was plotted as normalized fluorescence, i.e., $[F(t) - F(0)]/[F(\infty) - F(0)]$, versus time after photolysis (symbols) and fitted by Eq. 2 (lines). As an example three ghosts are shown with transport rate constants of 1.9×10^{-3} (●), 3.8×10^{-3} (■), and 5.6×10^{-3} (▲) s^{-1}, respectively, which closely correspond to the mean k values for ghosts with 1, 2, and 3 pores (cf. Fig. 3).
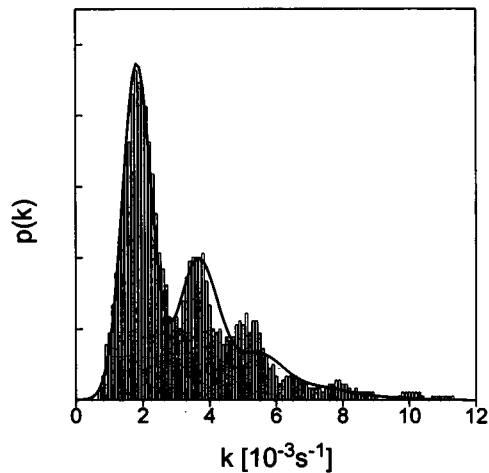
FIGURE 3 Optical single-channel analysis of the transport properties of the aerolysin pore for LY. The transport rate constant was determined for 260 individual ghosts, using the procedure shown in Fig. 2. The number of k-values found within a given k interval was then plotted versus k (bars). The k-value distribution shows discrete peaks, indicative of subpopulations of ghosts with a different number of pores. Only the peaks corresponding to cells with one or two pores are resolved, whereas peaks corresponding to higher pore numbers disappear in the noise. Fitting the experimental data by Eq. 14 (line) yielded a rate constant of ghosts with a single pore of $k(1)$ = $(1.83 \pm 0.43) * 10^{-3}$ s^{-1} and the mean number of pores per ghost, λ = 1.17.

Single-channel permeability of the aerolysin pore for calcium ions

In this case ghosts were loaded during preparation, i.e., after lysis and before resealing, with both a fluorescent calcium
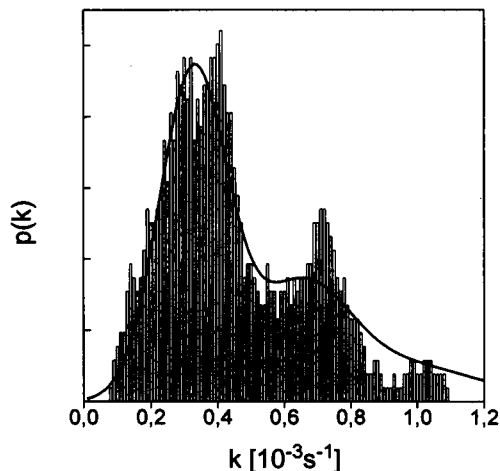
FIGURE 4 Optical single-channel analysis of the transport properties of the aerolysin pore for carboxyfluorescein (CF), another small hydrophilic organic fluorescent anion. The transport rate constant was determined for 130 individual ghosts, using the same procedure as in the case of LY. The distribution of k-values shows discrete peaks, indicative of subpopulations of ghosts with a different number of pores. Only the peaks corresponding to cells with one or two pores are resolved, whereas peaks corresponding to higher pore numbers disappear in the noise. Fitting the experimental data by Eq. 14 (line) yielded a rate constant of ghosts with a single pore of $k(1)$ = $(0.33 \pm 0.10) * 10^{-3}$ s^{-1} and the mean number of pores per ghost, λ = 1.00.

indicator (CG) and a caged calcium compound (DMN). After resealing, ghosts were treated with aerolysin at limiting concentrations. The ghost suspension was loaded into microslides and imaged in the confocal laser scanning microscope. At this stage, ghosts could be identified in the transmitted light image (Fig. 5 a) but hardly in the fluorescence image (Fig. 5 b), because the concentration of free Ca^{2+} was much smaller than the dissociation constant of CG. Upon illumination of the scanned field by a short pulse of UV light, Ca^{2+} was released and the intracellular phases became fluorescent (Fig. 5 c). It may be noted that the fluorescence varied between ghosts. This has previously been attributed to nonhomogeneous loading of ghosts with CG (Kubitscheck et al., 1995). The efflux of Ca^{2+} from ghosts into the medium was followed in a series of confocal images, examples of which are shown in Fig. 5, d–f.
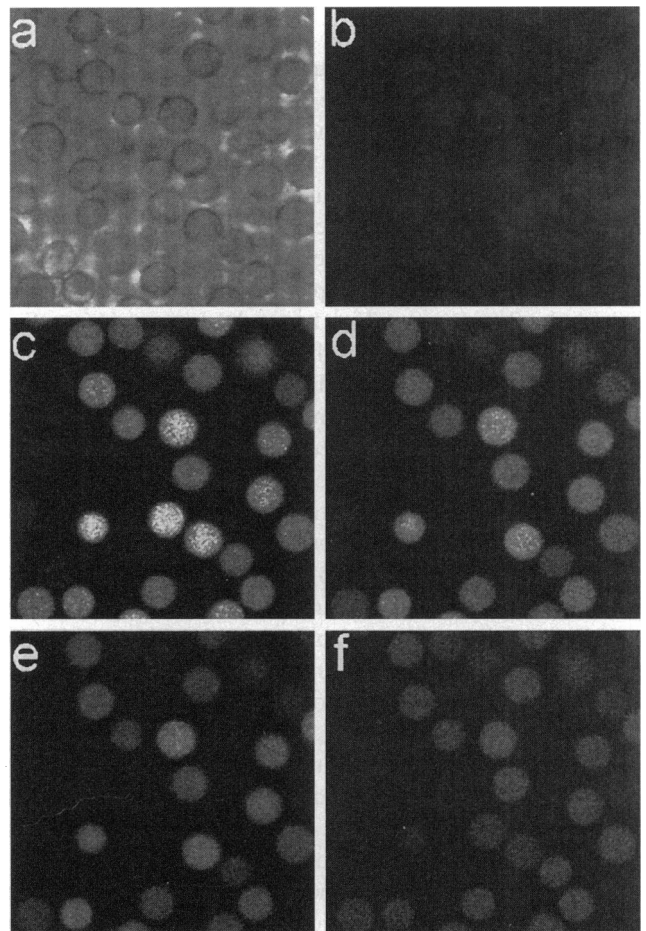
FIGURE 5 Fluorescence microphotolysis experiment to measure the membrane transport of Ca^{2+}, a nonfluorescent inorganic cation. Resealed human erythrocyte ghosts were loaded with the fluorescent calcium indicator calcium green (CG) and the caged calcium DMN and then treated with a limiting concentration of aerolysin to create about 1 pore/cell. (a) Transmitted light images of ghosts. (b) Confocal fluorescence image of ghosts before photolysis. Little fluorescence can be recognized because most of the Ca^{2+} is bound by DMN. (c–f) Fluorescence images acquired at 0, 10, 20, and 30 min after release of Ca^{2+} by a short pulse of UV light. The release of Ca^{2+} inside ghosts and the efflux into the Ca^{2+}-free medium can be recognized.

The outlined procedure should only be able to measure the transport of Ca^{2+} through the aerolysin pore if i) the untreated erythrocyte membrane is impermeable to Ca^{2+}, CG, and DMN and ii) the aerolysin pore is impermeable to CG and DMN but permeable for Ca^{2+}. The first condition was tested by loading ghosts with CG and DMN. The ghosts were imaged in the confocal microscope and Ca^{2+} was released by photolysis, without prior treatment with aerolysin. A series of images was acquired and evaluated for the mean intracellular fluorescence. In the course of 2 h only a very small decrease of the intracellular fluorescence was observed (Fig. 6 *a*), and the decrease in the first 30 min, the time interval used in the single channel analysis (Figs. 5, 7), was almost imperceptable. Of course, the erythrocyte membrane contains a very effective calcium pump which, in principle, could rapidly deplete the ghosts of Ca^{2+} (Kubits-check et al., 1995). However, the calcium pump was inactive under the conditions used because ATP was absent (Kubitscheck et al., 1995). The second condition was tested by loading ghosts with CG and free Ca^{2+}. Ghosts were then resealed and treated with aerolysin as described above for the single-channel analysis. After this, ghosts were resuspended in the same solution of CG and free Ca^{2+} used for loading. In the confocal microscope the ghosts were imaged, photobleached, and again imaged as described for LY and CF. Over a time interval of 2 h no influx of CG from the medium into the bleached ghosts could be detected (Fig. 6 *b*). In another series of experiments ghosts were at first loaded with CG and DMN, then resealed and treated with aerolysin. Finally they were carefully washed with CG-free and DMN-free buffer. They were then photolysed in the confocal microscope at different times after transfer into a DMN-free buffer. The level of intracellular fluorescence that could be induced (Fig. 6 *c*) remained constant in the first 2 h after transfer, indicating that the aerolysin pore was impermeable to DMN.

Having established that both the erythrocyte membrane and the aerolysin pore were impermeable to CG and DMN we proceeded in the same way as for LY and CF. A series of confocal images was acquired and evaluated for the intracellular fluorescence of individual ghosts. The fluorescence values were plotted and fitted according to Eq. 7. Examples of experimental data and fitted curves are given in Fig. 7. The three sample curves correspond to k-values of 7.9×10^{-3}, 14.7×10^{-3}, and 23.2×10^{-3} s^{-1} and thus to ghosts with 1, 2, or 3 pores, respectively. The k-values were plotted as histogram and fitted by Eq. 14. (Fig. 8).

A complete single-channel analysis was performed for two different aerolysin concentrations (Fig. 8). At the lower aerolysin concentration the first peak, representing ghosts with a single pore, was very prominent (Fig. 8 *a*) compared to the second peak, representing ghosts with two pores, and only very few higher k-values were observed. However, at the higher aerolysin concentration the second peak appeared considerably larger, and a continuum at higher k-values was also observed (Fig. 8 *b*). The fitting routine yielded a mean pore number of 0.56 for the lower and of 1.58 for the higher
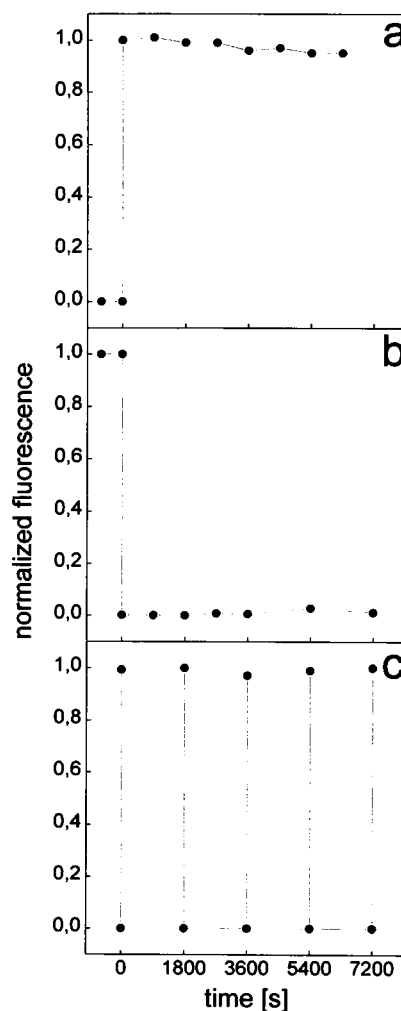

FIGURE 6   Control experiments to test whether (*a*) the erythrocyte membrane is virtually impermeable for Ca^{2+}, and (*b*, *c*) both the erythrocyte membrane and the aerolysin pore are impermeable for calcium green (CG) and DMN. (*a*) Ghosts were loaded with CG and DMN, but not treated with aerolysin. Ca^{2+} was released at time zero and ghosts were repetitively imaged. The mean intracellular fluorescence was derived from the images and plotted versus time. Little or no decrease of the intracellular fluorescence with time could be recognized, indicating that the erythrocyte membrane was virtually impermeable to Ca^{2+}. (*b*) Ghosts were loaded with CG and free Ca^{2+}, treated with aerolysin, and resuspended in a solution containing the same concentrations of CG and Ca^{2+}. Then, a transport measurement was performed essentially as in the case of LY (Fig. 2). In contrast to LY, however, the intracellular fluorescence of CG was not restored after photobleaching, indicating that the aerolysin pore was completely impermeable to CG. (*c*) Ghosts were loaded with CG and DMN, treated with aerolysin, and suspended in a buffer free of CG, DMN, and Ca^{2+}. At various times after transfer, Ca^{2+} was released in the intracellular compartments of ghosts by photolysis and the intracellular fluorescence was derived from confocal images. The same intracellular fluorescence was always elicited up to 2 h after transfer, indicating that the aerolysin pore was impermeable to DMN. In all cases shown the symbols represent the mean of approximately 10 individual values.

aerolysin concentration (Table 1), whereas the single-channel rate constants were $(7.8 \pm 1.85) \times 10^{-3}$ s^{-1} and $(8.20 \pm 2.3) \times 10^{-3}$ s^{-1}, and thus were indistinguishable within experimental accuracy. This was in perfect agreement with
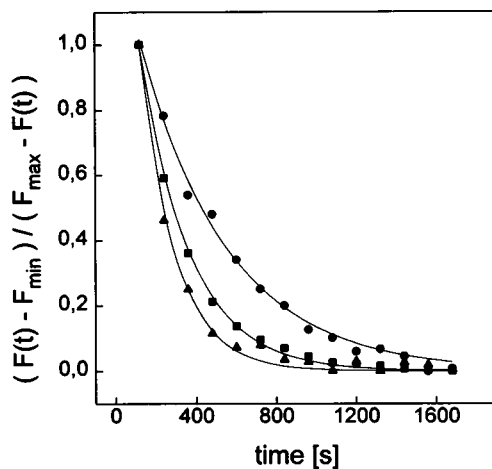
FIGURE 7 Examples of single-cell measurements to determine the transport rate constant for Ca^{2+}. A series of confocal images as shown in Fig. 5 was evaluated for the intracellular fluorescence of individual ghosts. The intracellular fluorescence was then plotted plotted as $[F(t) - F_{min}]/[F_{max} - F(t)]$ versus time after photolysis (symbols) and fitted by Eq. 7 (lines). As an example, the experimental values (symbols) of three ghosts are shown with rate constants of 7.9×10^{-3} (●), 14.7×10^{-3} (■), and 23.2×10^{-3} (▲) s^{-1}, respectively, which closely correspond to the mean k-values for ghosts with one, two, or three pores (cf. Fig. 8)

expectation, strengthening the confidence in the theoretical concept and its experimental realization, both of which are considerably more complex in the case of a nonfluorescent than a fluorescent transport substrate.

DISCUSSION

In the present study recently developed microscopic fluorescence methods were employed to subject the aerolysin pore in human erythrocyte membranes to an optical single-channel analysis. The single-channel rate constants obtained with LY, CF, and Ca^{2+} were used to derive the effective radius of the aerolysin pore according to Eq. 15. The outcome of these calculations is given in Table 2. The calculations assume a homogeneous population of cylindrical water-filled pores, a condition presumably approximated by the aerolysin pore (Wilmsen et al., 1992; Parker et al., 1994). The pore radius calculation also assumes that the transported substrate is a spherical molecule and that it is much smaller than the radius of the pore. Neither of these assumptions may be true in our studies. However, the influence of size of the molecule relative to the pore can be partially corrected for by taking steric hindrance at the pore entrance and viscous drag inside the pore into account according to Eq. 16 (Pappenheimer et al., 1951; Renkin, 1954; Paine and Scherr, 1975). The corrected radius of the aerolysin pore, derived in this manner, amounted to 23 Å, 22 Å, or 19 Å, using the rate constants of LY, CF, or Ca^{2+} (Table 2).

Interestingly, the corrected pore radius was about the same when derived from the data for LY and CF, in spite of the fact that the rate constants for these molecules differed
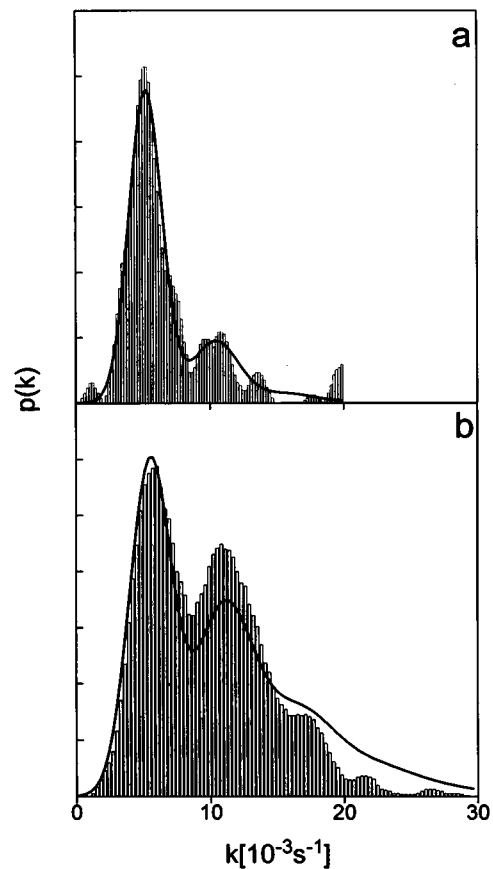

FIGURE 8 Optical single-channel analysis of the transport properties of the aerolysin pore for Ca^{2+}. (a) and (b) pertain to ghost suspensions treated with different aerolysin concentrations (about 75 and 150 ng/ml). In both cases the transport rate constant was determined for a large number of individual ghosts using the procedure shown in Fig. 7. The number of k-values found within a given k interval was then plotted versus k (bars). The k-value distribution shows discrete peaks, indicative of subpopulations of ghosts with a different number of pores. Only the peaks corresponding to cells with one opr two pores are clearly resolved, whereas peaks corresponding to higher pore numbers disappear in the noise. Fitting the experimental data by Eq. 14 (line) yielded the rate constant of ghosts with a single pore to be $(7.8 \pm 1.85) \times 10^{-3}$ s^{-1} (a) and $(8.20 \pm 2.3) \times 10^{-3}$ s^{-1} (b) and the mean number of pores per ghost to be 0.56 (a) and 1.58 (b).

by a factor of 5.5. On the other hand, the corrected pore radius derived from the Ca^{2+} data was slightly smaller. This may be because the Pappenheimer-Renking correction described above does not account for fixed charges on the pore wall. Previous conductance measurements of the aerolysin pore reconstituted in planar lipid bilayers suggested a slight anion preference with a Cl^-/Na^+ permeability ratio of 3.6:1 (Wilmsen et al., 1990), and this likely explains the differences between pore radius values derived from flux of the two organic anions and Ca^{2+}. In any case, our results suggest that the aerolysin pore in the erythrocyte membrane has a radius between 19 and 23 Å, in reasonably good agreement with the estimate of an upper limit of 15 Å based on the permeability of erythrocytes containing aerolysin channels to peptides of different sizes (Howard and Buckley, 1982).

TABLE 2 Functional and structural properties of the aerolysin pore as derived from the optical single-channel analysis

	Lucifer yellow	Carboxy-fluorescein	Ca^{2+}
Molecular mass (Da)	457	376	40
Diffusion coefficient* ($\mu m^2 s^{-1}$)	275	217	740
Effective molecular radius[‡] (Å)	7.8	10	2.9
Single-channel rate constant ($10^{-3} s^{-1}$)	1.83	0.33	8.0
Flux per pore[§] (molecules s^{-1} mM^{-1})	72,000	13,000	312,000
Pore radius[¶] (Å)			
Effective	9.8	5.0	13.2
Corrected	23	22	19

* Lateral diffusion coefficent D in water at 23°C. Values are taken from Peters et al. (1990) for Lucifer yellow, from Blonk et al. (1992) for carboxyfluorescein, and from Allbritton et al. (1992) for Ca^{2+}.

[‡] For Lucifer yellow and Ca^{2+} a hydrodynamic radius a was dervived from the diffusion coefficient according to $a = kT/6\pi\eta D$. The value for carboxyfluorescein was taken from Blonk et al. (1992), who determined an overall a of fluorescein isothiocyanate by molecular modeling. We assume here that both a and the diffusion coefficient of flurorescein isothiocyanate and carboxyflurorescein are virtually identical.

[§] At a concentration difference across the membrane of 1 mM.

[¶] The effective radius was calculated according to Eq. 13 with $\Delta x = 80$ Å. The corrected radius was derived according to Eq. 14, taking steric hindrance and viscous drag according to Pappenheimer et al. (1951), Renkin (1954), and Paine and Scherr (1975) into account.

In the cytosol of resting cells the concentration of free Ca^{2+} is normally kept at a low level (<0.1 μM), and elevations of Ca^{2+} concentration are tightly controlled in time and space to regulate a large number of metabolic reactions (for a review, see Petersen et al., 1994). In contrast, the extracellular Ca^{2+} concentration usually amounts to >1 mM. Using the results of the present study it is possible to estimate what effect the insertion of a single pore into the plasma membrane would have on erythrocyte Ca^{2+} homeostasis. Assuming that the Ca^{2+} concentration difference across the plasma membrane amounts to 1 mM, application of Eq. 10 with $V_{ghost} = 65$ fl (Kubitscheck et al., 1995) yields a flux of about 300,000 calcium ions per aerolysin pore per second. The corresponding values for LY and CF are listed in Table 2. This calcium flux rate implies (Eq. 1) that after insertion of a single aerolysin pore into the membrane of an erythrocyte ghost, the intracellular calcium concentration would increase at an initial rate of 8 μM every second. Ca^{2+} levels would continue to rise rapidly for several minutes, then increase less rapidly, reaching a constant level about 10 min after the channel was formed (cf. Fig. 7). In intact erythrocytes, the increase in the intracellular Ca^{2+} concentration would be dampened by Ca^{2+} export via the plasma membrane calcium pump (PMCA). However, the maximum pumping rate of the PMCA is only about 50 calcium ions per active PMCA monomer per

second, or 40,000 calcium ions per erythrocyte per second, as determined recently (Kubitscheck et al., 1995). Thus the total pool of PMCA molecules in the erythrocyte would not nearly be sufficient to counteract the effect of a single aerolysin pore. In other cell types, any Ca^{2+} increase would also be reduced by calcium buffers, which typically are present at cytosolic concentrations of up to 300 μM (Allbriton et al., 1992), as well as by calcium uptake into intracellular stores. However, because a sudden and permanent rise in the cytosolic Ca^{2+} concentration above ~1 μM is sufficient to rapidly trigger necrotic and apoptotic death (Orrenius et al., 1989; Nicotera et al., 1994), a single aerolysin pore would obviously be an immediate and severe threat to sensitive cells.

On the other hand, osmotic effects, which are usually said be the major cause of cell death by pore-forming proteins, develop much more slowly. For example, in erythrocytes hemolysis is only 10% complete 25 min after the addition of enough aerolysin to generate approximately 1 pore/cell (not shown here). This was determined by measuring the increase in transmission of a 2% erythrocyte suspension at 800 nm (room temperature). Other cell types might be able to remove aerolysin channels by proteolysis or endocytosis over such a long time scale and thereby resist death due to changes in osmotic pressure. Thus our results and calculations lead to the conclusion that at very low toxin concentration, as it is likely to be in an infected host, cells are more likely to succumb to a disturbance in intracellular Ca^{2+} homeostasis than to osmotic imbalance.

Finally, it may be pointed out that the results reported in this paper suggest that OSCA is not restricted to the characterization of aerolysin pores but can be applied to many other problems. The functional analysis of membrane transporters by electrical measurements of single-channel events is widely used and has had a decisive impact on membrane biology (for a review, see Sakmann and Neher, 1991). The major domain of the electrical signal analysis is the fast transport of small anorganic ions through transmembrane channels. The optical single-channel analysis, in comparison, can provide data on the transport of small and large, charged and uncharged, fluorescent and nonfluorescent substrates (Peters et al., 1990; Sauer et al., 1991). Moreover, OSCA is probably sensitive enough to detect small fluxes such as those mediated by carriers and pumps, and, based on fluorescence detection, OSCA should be able to simultaneously follow the flux of two or more transport substrates. On the other hand, the time resolution of OSCA is smaller than that of electrical recordings and it may be difficult to pick up by OSCA channel opening and closing.

REFERENCES

Allbriton, N. L., T. Meyer, and L. Stryer. 1992. Range of messenger action of calcium ion and inositol 1,4,5-triphosphate. *Science*. 258:1812–1815.

Axelrod, D., D. E. Koppel, J. Schlessinger, E. Elson, and W. W. Webb. 1976. Mobility measurement by analysis of fluorescence photobleaching recovery kinetics. *Biophys. J.* 16:1055–1069.

Blonk, J. C. G., A. Don, H. van Alst, and J. J. Birmingham. 1993. Fluorescence photobleaching recovery in the confocal scanning microscope. *J. Microsc.* 169:363–374.

Buckley, J. T. 1990. Purification of cloned proaerolysin released by a low protease mutant of *Aeromonas salmonicida. Biochem. Cell Biol.* 68: 221–224.

Dennert, G., and E. R. Podack. 1983. Cytolysis by H-2-specific T killer cells. *J. Exp. Med.* 157:1483–1495.

Howard, S. P., and J. T. Buckley. 1982. Membrane glycoprotein receptor and hole-forming properties of a cytolytic protein toxin. *Biochemistry.* 21:1662–1667.

Jacobson, K., E. Wu, and G. Poste. 1976. Measurement of the translational mobility of concanavalin A in glycerol-saline solutions and on the cell surface by fluorescence recovery after photobleaching. *Biochim. Biophys. Acta.* 433:215–222.

Kaplan, J. H., B. Forbush, and J. F. Hoffman. 1978. Rapid photolytic release of adenosine 5′-triphosphate from a protected analogue: utilization by the Na:K pump of human red blood cell ghosts. *Biochemistry.* 17:1929–1935.

Kubitscheck, U., L. Pratsch, H. Passow, and R. Peters. 1995. Calcium pump kinetics determined in single erythrocyte ghosts by microphotolysis and confocal imaging. *Biophys. J.* 69:30–41.

Menestrina, G. 1994. Pore-forming toxins and antimicrobial polypeptides. *Toxicol. Appl. Pharmacol.* 87:1–268.

Nicotera, P., B. Zhivotovsky, and S. Orrenius. 1994. Nuclear calcium transport and the role of calcium in apoptosis. *Cell Calcium.* 16: 279–288.

Orrenius, S., D. J. McConkey, G. Bellomo, and P. Nicotera. 1989. Role of Ca2+ in toxic cell killing. *Trends Biochem. Sci.* 10:281–285.

Paine, P. L., and P. Scherr. 1975. Drag coefficients for the movement of rigid spheres through liquid-filled cylindrical pores. *Biophys. J.* 15: 1087–1091.

Pappenheimer, J. R., E. M. Renkin, and L. M. Borrero. 1951. Filtration, diffusion and molecular sieving through peripheral capillary membranes. *Am. J. Physiol.* 167:13–23.

Parker, M. W., J. T. Buckley, J. P. M. Postma, A. D. Tucker, K. Leonard, F. Pattus, and D. Tsernoglou. 1994. Structure of *Aeromonas* toxin proaerolysin in its water-soluble and membrane-channel states. *Nature.* 367:292–295.

Peters, R. 1983. Nuclear envelope permeability measured by fluorescence microphotolysis of single liver cell nuclei. *J. Cell Biol.* 258: 11427–11429.

Peters, R. 1984. Nucleo-cytoplasmic flux and intracellular mobility in single hepatocytes measured by fluorescence microphotolysis. *EMBO J.* 3:1831–1836.

Peters, R., J. Peters, K. H. Tews, and W. Bähr. 1974. A microfluorimetric study of translational diffusion in erythrocyte membranes. *Biochim. Biophys. Acta.* 367:282–294.

Peters, R., H. Sauer, J. Tschopp, and G. Fritzsch. 1990. Transients of perforin pore formation observed by fluorescence microscopic single channel recording. *EMBO J.* 9:2447–2451.

Peters, R., and M. Scholz. 1991. Fluorescence photobleaching techniques. *In* New Techniques of Optical Microscopy and Microspectroscopy. R. J. Cherry, editor. Macmillan Press, Houndsmill. 199–228.

Petersen, O. H., C. C. H. Petersen, and H. Kasai. 1994. Calcium and hormone action. *Annu. Rev. Physiol.* 56:297–319.

Renkin, E. M. 1954. Filtration, diffusion, and molecular sieving through porous cellulose membrane. *J. Gen. Physiol.* 38:225–243.

Sakmann, B., and E. Neher. 1991. Single-Channel Recording. Plenum Press, New York and London.

Sauer, H., L. Pratsch, G. Fritzsch, S. Bhakdi, and R. Peters. 1991. Complement pore genesis observed in erythrocyte membranes by fluorescence microscopic single-channel recording. *Biochem. J.* 276:395–399.

Schwoch, G., and H. Passow. 1973. Preparation and properties of human erythrocyte ghosts. *Mol. Cell. Biochem.* 2:197–218.

Tsien, R. Y., T. Pozzan, and T. J. Rinke. 1984. Measuring and manipulating cytosolic Ca²⁺ with trapped indicators. *Trends Biochem. Sci.* 263–266.

van der Goot, F. G., F. Pattus, M. Parker, and J. T. Buckley. 1994. The cytolytic toxin aerolysin: from the soluble form to the transmembrane channel. *Toxicology.* 87:19–28.

Wedekind, P., U. Kubitscheck, and R. Peters. 1994. Scanning microphotolysis: a new photobleaching technique based on fast intensity modulation of a scanned laser beam and confocal imaging. *J. Microsc.* 176:23–33.

Wilmsen, H. U., J. T. Buckley, and F. Pattus. 1991. Site-directed mutagenesis at histidines of aerolysin from *Aeromonas hydrophila*: a lipid planar bilayer study. *Mol. Microbiol.* 5:2745–2751.

Wilmsen, H. U., K. R. Leonard, W. Tichelaar, J. T. Buckley, and F. Pattus. 1992. The aerolysin membrane channel is formed by heptamerization of the monomer. *EMBO J.* 11:2457–2463.

Wilmsen, H. U., F. Pattus, and J. T. Buckley. 1990. Aerolysin, a hemolysin from *Aeromonas hydrophilia*, forms voltage-gated channels in planar lipid bilayers. *J. Membr. Biol.* 115:71–81.